

Real-time breath gas analysis of CO and CO₂ using an EC-QCL

Ramin Ghorbani¹ · Florian M. Schmidt¹ 

Received: 31 January 2017 / Accepted: 29 March 2017 / Published online: 18 April 2017
© The Author(s) 2017. This article is an open access publication

Abstract Real-time breath gas analysis is a promising, non-invasive tool in medical diagnostics, and well-suited to investigate the physiology of carbon monoxide (CO), a potential biomarker for oxidative stress and respiratory diseases. A sensor for precise, breath-cycle resolved, simultaneous detection of exhaled CO (eCO) and carbon dioxide (eCO₂) was developed based on a continuous wave, external-cavity quantum cascade laser (EC-QCL), a low-volume multi-pass cell and wavelength modulation spectroscopy. The system achieves a noise-equivalent (1σ) sensitivity of $8.5 \times 10^{-8} \text{ cm}^{-1} \text{ Hz}^{-1/2}$ and (2σ) detection limits of 9 ± 2 ppbv and 650 ± 7 ppmv at 0.14 s spectrum acquisition time for CO and CO₂, respectively. Integration over 15 s yields a precision of 0.6 ppbv for CO. The fact that the eCO₂ expirograms measured by capnography and laser spectroscopy have essentially identical shape confirms true real-time detection. It is found that the individual eCO exhalation profiles from healthy non-smokers have a slightly different shape than the eCO₂ profiles and exhibit a clear dependence on exhalation flow rate and breath-holding time. Detection of indoor air CO and broadband breath profiling across the 93 cm^{-1} mode-hop-free tuning range of the EC-QCL are also demonstrated.

1 Introduction

Sensitive trace species detection with high accuracy, precision and time resolution is important in many scientific and industrial applications. With the advent of tunable semiconductor lasers operating in the mid-infrared, i.e. quantum cascade lasers (QCLs) and interband cascade lasers (ICLs), suitable optical sensors can be realized based on tunable diode laser absorption spectroscopy (TDLAS) or cavity-enhanced methods [1, 2]. In TDLAS, high sensitivity is achieved employing multi-pass cells (MPCs) [3] for path length enhancement and modulation techniques, e.g. wavelength modulation spectroscopy (WMS) [4], for noise reduction. Installed in an external-cavity containing a wavelength-selective device, a QCL can provide single-mode operation with narrow linewidth and high output power in a large part of its broad gain profile. Such external-cavity QCLs (EC-QCLs) also offer a large ($\sim 100 \text{ cm}^{-1}$) mode-hop-free tuning range and high-bandwidth fine tuning via piezoelectric elements and laser injection current [1, 5]. Consequently, EC-QCLs have been used for high-resolution broadband absorption spectroscopy [6, 7], as well as for sensitive narrowband detection in environmental, combustion and medical applications [8–13]. Given the high output power, EC-QCLs are also well-suited for photo-acoustic spectroscopy [14].

An emerging application of great interest is the measurement of molecular biomarkers in exhaled breath to non-invasively assess the physiological and metabolic state of the body [15, 16]. Breath gas analysis (BGA) puts high demands on the analytical equipment as it requires high sensitivity (typically low biomarker concentrations), high selectivity (>200 trace species in breath) and adequate, well-designed breath sampling systems [15]. Ideally, since

This article is part of the topical collection “Field Laser Applications in Industry and Research” guest edited by Francesco D’Amato, Erik Kerstel, and Alan Fried.

✉ Florian M. Schmidt
florian.schmidt@umu.se

¹ Department of Applied Physics and Electronics, Umeå University, SE-90187 Umeå, Sweden

for many potential biomarkers origin and biochemical pathways are not well known, the instruments should also enable reliable and systematic physiological studies. The main techniques used in BGA are gas chromatography coupled to mass spectrometry (GC-MS), selected-ion flow-tube MS (SIFT-MS), proton-transfer-reaction MS (PTR-MS) [17], solid-state gas sensors [18] and laser spectroscopy [19]. Breath sampling traditionally involves collecting end-tidal or mixed breath into containers, such as polymer bags, possibly sample storage and pre-treatment, and subsequent offline analysis.

Real-time BGA implies online breath sampling with sub-second gas exchange and data acquisition times in order to resolve individual exhalation profiles (or expirograms) of biomarkers. The advantages compared to offline analysis are that (1) additional information is obtained, since the time-resolved concentration during exhalation carries spatial information about the respiratory tract and lung; (2) transient phenomena and fast changes in response to interventions, e.g. treatment, exposure and stable isotope tracer intake, can be resolved; (3) the optimization of breath sampling and reliable analysis are facilitated, and (4) biomarker expirograms and intervention response can be compared to physiological and pharmacokinetic models, respectively [20, 21], and used to extract physiological parameters. True real-time detection requires a sampling and analysis system with low volume to ensure fast gas exchange times. Breath-cycle resolved, simultaneous detection of 1–3 compounds can today be achieved with the soft-ionization MS techniques [22, 23] and laser spectroscopy [24–27], but only the latter method also offers the potential for compact and affordable instrumentation, which is desired in medical research and clinical practice.

Endogenous carbon monoxide (CO) is a by-product of systemic heme oxygenase and thus considered a potential marker for oxidative stress, inflammation and respiratory diseases [28]. Most of the CO is bound to blood hemoglobin and released via the breath following gas exchange at the alveolar interface. The normal range for end-tidal exhaled CO (eCO) concentrations of healthy non-smokers is 1–3 parts per million by volume (ppmv). Increased levels have been observed in smokers and diseased cohorts, but the usefulness of eCO to diagnose respiratory diseases, such as asthma, chronic obstructive pulmonary disease and cystic fibrosis is currently under debate [29]. Because the systemic eCO contribution from the alveoli is large and eCO is heavily influenced by inhaled CO (e.g. cigarette smoke, air pollution, indoor air), it is questionable whether a small contribution to eCO due to local oxidative stress or inflammation in the airways can be detected [28]. Precise real-time BGA and the ability to measure the inhaled CO concentration could be a way to distinguish between the eCO sources. Gas exchange in the airways is usually

indicated by a flow-rate dependence of the exhalation profiles [30]. Due to its low proton affinity, CO is rarely measured with standard soft-ionization MS, and eCO detection with solid state, chemiluminescence and near-infrared sensors lacks the required time-resolution for real-time BGA [31]. Recent efforts with laser spectroscopy [25, 32–34] revealed controversial results regarding the dependence of eCO on exhalation flow rate and breath-holding time.

Exhaled carbon dioxide (eCO₂), with expected end-tidal concentrations of 5–6%, can be used as an indicator for the integrity of a breath sample (hyperventilation, dilution) and for normalization to reduce inter-individual variations. A comparison between eCO₂ in the sample cell and from capnography close to the mouth can help to validate real-time detection and to determine possible delays in the sampling system.

In this work, we report on and characterize a mid-infrared TDLAS sensor for real-time detection of CO and CO₂ in exhaled breath. The system combines an EC-QCL with a robust, low-volume MPC and takes advantage of various laser wavelength tuning mechanisms to perform broadband breath profiling with direct absorption spectroscopy (DAS), as well as sensitive narrowband detection with WMS. The high sensitivity and precision of WMS enables quantification of indoor air CO and the precise measurement of individual eCO and eCO₂ exhalation profiles. The dependence of profile shape and end-tidal eCO on exhalation flow rate and breath-holding time is investigated for two healthy non-smokers and compared to the corresponding eCO₂ expirograms.

2 Experimental TDLAS setup and breath sampler

A water-cooled, continuous wave (cw) EC-QCL (Daylight solutions, TLS-41047-MHF) in Littrow configuration provided single-mode laser output in the wavelength range 2015–2220 cm⁻¹ (4.50–4.96 μm) and a peak output power of 160 mW. The external cavity included a diffraction grating on a rotating platform. The laser wavelength could be tuned using three different mechanisms: (1) rotation of the grating with a motor in step mode (discrete steps of down to 0.01 cm⁻¹) or in continuous sweep scan mode (~10 cm⁻¹/s), (2) rotation of the grating with a piezoelectric element (PZT) and (3) via the injection current. The wide 205 cm⁻¹ overall accessible range included a 93 cm⁻¹ mode-hop-free tuning range from 2080 to 2173 cm⁻¹ (4.602–4.808 μm). The grating step/sweep motor was operated via the laser temperature and current controller (Daylight solutions, 1001-TLC), while the PZT on the grating was driven by a high-voltage amplifier (Piezosystem Jena, 30V300 CLE) that enabled a continuous scan over 1.9–0.7 cm⁻¹ for frequencies of 100–500 Hz. The maximum

tuning range accessible by injection current modulation was 0.18 cm^{-1} . The wavelength tuning properties of the EC-QCL are summarized in Table 1.

Using an appropriate focusing lens, the light from the EC-QCL was coupled to a circular multi-pass cell (MPC, IR Sweep, IRcell-4M) [3] with an effective path length of 3.99 m (51-reflections), a volume of 38 ml and a specified, lowest achievable fringe-level of 0.39% rms of the dc intensity. The output beam of the MPC was focused on a mid-infrared photodetector (VIGO System, PVI-2TE-5-1 \times 1). Prior to the MPC the light passed through a variable attenuator needed to reduce the laser power to within the operating range of the detector (<1 mW). An uncoated solid Germanium etalon (LightMachinery, OP-5483-50.8) with a free-spectral-range of 734.2 MHz was used to record the relative frequency scale of the laser scan. The detector signal was acquired by a 60-MHz bandwidth, 16-bit data acquisition system (Spectrum, M2i.4963-exp) integrated in a PC and controlled by a Labview program. A schematic drawing of the experimental setup is shown in Fig. 1a.

The MPC outlet was connected to a diaphragm vacuum pump (Leybold, Divac 1.4HV3C), which provided a maximum pumping speed of 360 ml/s down to 50 Torr. The pressure in the cell was monitored by a pressure gauge (Leybold, Ceravac CTR100) and set to 100 Torr using a shut-off valve (Swagelok, EL3233) at the MPC inlet. Calibration curves for CO and CO₂ were determined using standard

gases containing $29.0 \pm 2 \text{ ppmv CO}$ and $9.01 \pm 2\% \text{ CO}_2$, and subsequent dilution with dry air using mass flow controllers (MKS Instruments, GM50A).

For online breath gas analysis, a breath sampling device was connected to the MPC inlet. The breath sampler (Fig. 1b) consisted of a buffer tube of length 15 cm and volume 30 ml. A disposable anti-bacterial filter (GVS, Eco Maxi Electrostatic Filter, 4222/701), a capnograph (Phillips Respironics, Capnostat 5) and a flow meter (Phillips Respironics, FloTrak Elite) were attached to the buffer tube inlet. The anti-bacterial filter also served as a mouth piece. Important sampling parameters (flow rate, tidal volume, eCO₂, eCO and time) could be visually followed in real-time on a screen to facilitate keeping inhalation and exhalation volumes and breathing frequency constant, and thereby improve sampling repeatability. The volumes of sampling system and MPC matched the vacuum pumping speed at 100 Torr such that the gas exchange time in the cell was around 0.1 s and similar to the spectrum acquisition time (0.14 s). This implied that the breath in the buffer tube at atmospheric pressure was drawn to the MPC at a flow rate of 50 ml/s, enabling true real-time sampling for exhalation flow rates down to this value. For some experiments, orifices with diameters of 1, 2 and 2.5 mm were attached to the end of the buffer tube via a 2-way valve (Rudolph Inc.) to restrict the exhalation flow rate to constant values of about 80, 160 and 250 ml/s, respectively. The 2-way valve

Table 1 EC-QCL wavelength tuning properties

Tuning	Range (cm ⁻¹)	Bandwidth	Function	Mechanism
Total	2015–2220	~10 cm ⁻¹ /s	Linear, step/sweep	Grating rotation
Mode-hop-free	2080–2173	~10 cm ⁻¹ /s	Linear, step/sweep	Grating rotation
PZT fine	1.9	100 Hz	Sinusoidal, 0 to 100 V	Grating rotation
	0.7	500 Hz		
Current fine	0.18	1 MHz	Sinusoidal, -2 to 2 V	Injection current

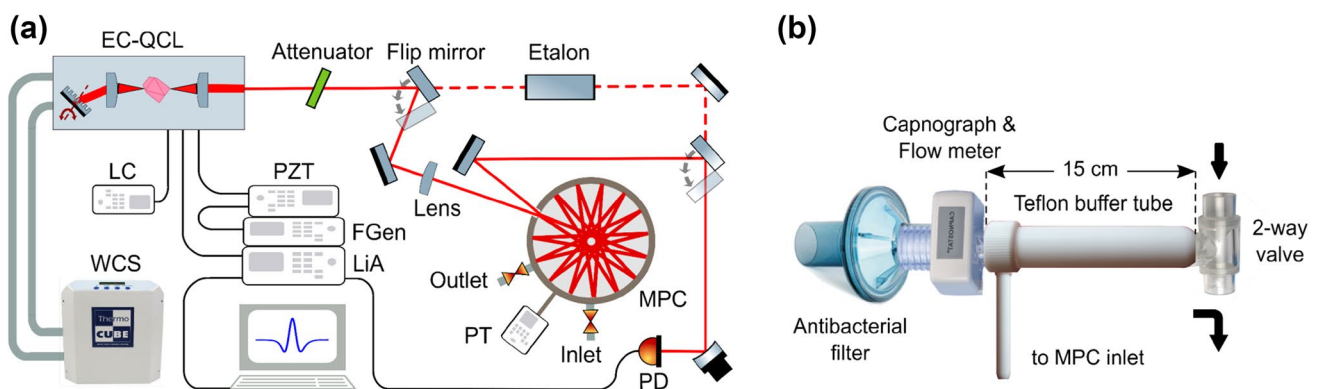


Fig. 1 Schematic drawings of the experimental TDLAS setup around the EC-QCL (a) and the breath sampler (b). LC laser current and temperature controller, PZT piezo amplifier, FGen function generator,

LiA lock-in amplifier, WCS water cooling system, MPC multi-pass cell, PT pressure transducer, PD photodetector

provided separate routes for exhalation and (unrestricted) inhalation. This resulted in rapid flushing of the buffer tube with air during inhalation, and thus a better definition of the end of exhalation, and proper measurements of indoor air CO and the next exhalation profile [35].

Broadband spectroscopy was performed by continuously scanning the EC-QCL over its entire mode-hop-free range using the built-in stepper motor function in sweep mode. Each sweep scan took around 10 s. The spectral resolution was 30 MHz, depending on the sweep scan speed ($10 \text{ cm}^{-1}/\text{s}$) and number of data points acquired (90 k). The nitrogen-filled MPC background signal and Beer-Lambert's law were used to derive the absorbance. The background was wavelength-dependent due to fringes from the optical components in the setup, including the external cavity of the laser and the MPC. Because the fine tuning options were deactivated in cw sweep mode, it was not possible to perform WMS. While the absolute wavelength range was constant for each scan, the scan duration was not repeatable. Since the grating motor could not be triggered to record the same wavelength at a given time, the separately measured background signals were different from the analytical background, which caused noise in the final spectrum. For the same reason, the relative frequency scale was slightly incorrect. The raw data were post-processed in Matlab using smoothing, interpolation and uniform resampling of data points to adjust the background prior to absorbance calculation. The absolute frequency scale was calibrated via a single CO peak using the HITRAN 2012 database [36].

Narrowband DAS detection around 2119.6 cm^{-1} was achieved by scanning the laser wavelength via the PZT with a 70-Hz sinusoidal waveform provided by a function generator (Agilent 33522A). Voigt lineshape functions simulated using Beer-Lambert's law were least-squares fitted to the raw spectra (10 averages) with line center frequency, collisional broadening, concentration and baseline

offset as free fitting parameters. The nitrogen-filled MPC background was measured separately and included in the fitting routine. To perform WMS, an additional 47.7 kHz sinusoidal waveform generated by an external lock-in amplifier (Stanford Research Systems, SR830 DSP) was fed to the injection current input of the EC-QCL. The modulation amplitude was optimized for $2f$ -WMS detection of the employed CO absorption line. The detector signal was sent to the lock-in amplifier for demodulation at twice the modulation frequency (95.4 kHz). $2f$ -WMS Voigt lineshape functions calculated using the approach by Westberg et al. [37] were least-squares fitted to the raw WMS spectra (10 averages) with line center frequency, amplitude, collisional broadening, modulation amplitude and baseline offset as free (in a narrow range) fitting parameters. The peak values extracted from the fits were compared to a calibration curve to obtain the concentrations. The $2f$ -WMS background signal of the nitrogen-filled MPC was recorded separately for each measurements series and subtracted from the analytical $2f$ -WMS signal prior to curve fitting.

3 Broadband spectroscopy and line selection

In order to demonstrate broadband spectroscopy with the EC-QCL, and to facilitate line selection for narrowband detection, DAS spectra over the mode-hop-free tuning range were recorded (no averaging) for two different samples: a mixture of the CO and CO₂ standard gases (Fig. 2) and end-tidal breath of a healthy non-smoker (Fig. 3). The figures also show a smaller section of the broadband scan in more detail (Figs. 2b, 3b). In the standard sample, concentrations of 28.5 ppmv CO and 6% CO₂ were used. The concentrations for CO, CO₂ and water (H₂O) found in the breath sample were 1.2 ppmv, 5% and 1.1%, respectively. No other species have been identified in this region. The lower part of each graph

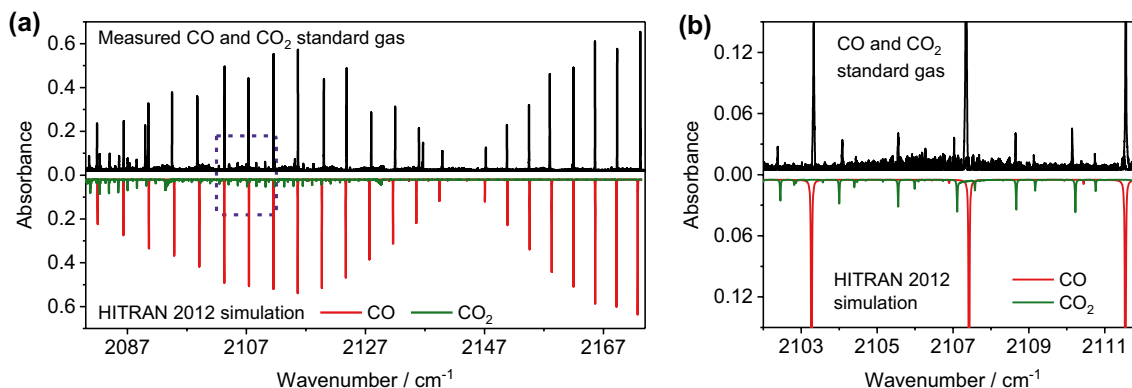


Fig. 2 **a** Broadband mode-hop-free EC-QCL scan over 93 cm^{-1} for a mixture of CO (28.5 ppmv) and CO₂ (6%) standard gases (pressure 100 Torr), together with a corresponding HITRAN 2012 simulation. **b** Section of the broadband scan around 2107 cm^{-1}

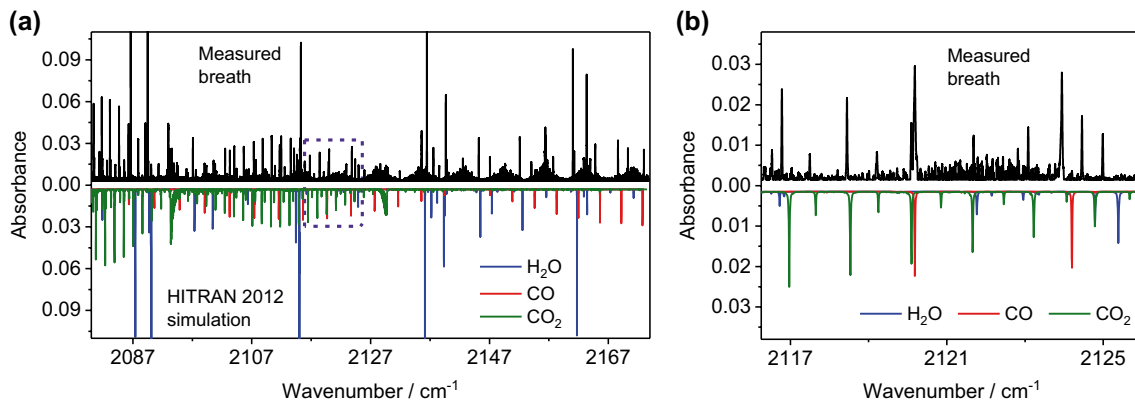


Fig. 3 **a** Broadband mode-hop-free EC-QCL scan over 93 cm^{-1} for an end-tidal breath sample (pressure 100 Torr) of a healthy non-smoker, together with a corresponding HITRAN 2012 simulation for

1.2 ppmv CO , $5\% \text{ CO}_2$ and $1.1\% \text{ H}_2\text{O}$. **b** Section of the broadband scan around the spectral region used for narrowband WMS detection

displays a corresponding simulated spectrum based on the HITRAN 2012 database [36].

In general, there is a good agreement between experiment and simulation. In both figures, there are visible errors in the frequency scale, caused by the poor repeatability of the sweep scan. The baseline noise arises as a consequence of changes in the separately measured background. In the standard sample, the fundamental band of CO and some CO₂ lines are clearly visible. A small amount of H₂O was also present. In the breath sample spectra, absorption lines from H₂O, CO and CO₂ can be distinguished. The H₂O concentration (1.1%) is lower than that expected in breath (5%). This is probably due to condensation in the unheated breath sampling system. Since CO and CO₂ are molecules with low water-solubility, it is assumed that the condensation does not affect eCO and eCO₂ quantification.

The selection of suitable absorption lines for simultaneous CO and CO₂ detection in breath was based on the criteria that (1) the line strengths allow quantification in the expected eCO and eCO₂ concentration ranges, (2) the line separation is large enough to avoid significant spectral overlap at a pressure of 100 Torr, but sufficiently small to fit within the PZT scan range and (3) there is no spectral interference with H₂O. The P(6) line of CO at 2119.681 cm^{-1} with a line strength of $3.709 \times 10^{-19} \text{ cm}^{-1}/(\text{molecule cm}^{-2})$ and the P(13e) line of CO₂ at $2119.596413 \text{ cm}^{-1}$ with a line strength of $9.425 \times 10^{-24} \text{ cm}^{-1}/(\text{molecule cm}^{-2})$ were found to fulfill these conditions. A section of the broadband breath scan around this spectral region is shown in Fig. 3b together with a HITRAN simulation. In the following, these two absorption lines are used for narrowband spectroscopy and real-time breath gas analysis.

4 Sensor performance—narrowband detection

Figure 4 presents typical DAS (panel a) and $2f$ -WMS (panel b) signals (red solid markers) from the selected spectral region near 2119.6 cm^{-1} recorded during online breath sampling (healthy non-smoker). The graphs also show least-square curve fits (solid blue line) of Voigt line-shapes to the raw data (10 averages, 0.14 s time resolution). The fit residuals are shown in the panels below. The CO and CO₂ concentrations determined by the fit (and by calibration) were 1.1 ppmv and 5.9%, respectively. The breath sample was assumed to rapidly cool down to near-room temperature on its way to the MPC. Spectral interference due to sample humidity (max. 1.1% H₂O in the cell) was not observed (see also Fig. 3b).

The signal-to-noise ratio (2σ) of the DAS spectrum (Fig. 4a) was 12, which gives a sensitivity of $1.8 \times 10^{-6} \text{ cm}^{-1} \text{ Hz}^{-1/2}$ and detection limits of 96 parts per billion by volume (ppbv) for CO and 0.5% for CO₂. The noise equivalent (1σ) sensitivity determined for $2f$ -WMS detection is $8.5 \times 10^{-8} \text{ cm}^{-1} \text{ Hz}^{-1/2}$ and the (2σ) signal-to-noise ratio is 127, thus yielding detection limits of 9 ppbv and 650 ppmv for CO and CO₂, respectively. DAS is limited by $1/f$ -noise, and WMS is limited by fluctuation in the wavelength-dependent background signal caused by $1/f$ -noise coupling in via fringes. The etalons originate partly from the EC-QCL, but also other optical compounds in the system, including the MPC. The overall fringe level in the WMS spectra was 0.42% rms of the dc intensity. The improvement achieved with WMS compared to DAS was about 10.

Figure 5a shows Allan-Werle deviation plots for DAS and WMS detection recorded at concentrations of 1.3 ppmv CO and 0.2% CO₂. For both gases, the WMS

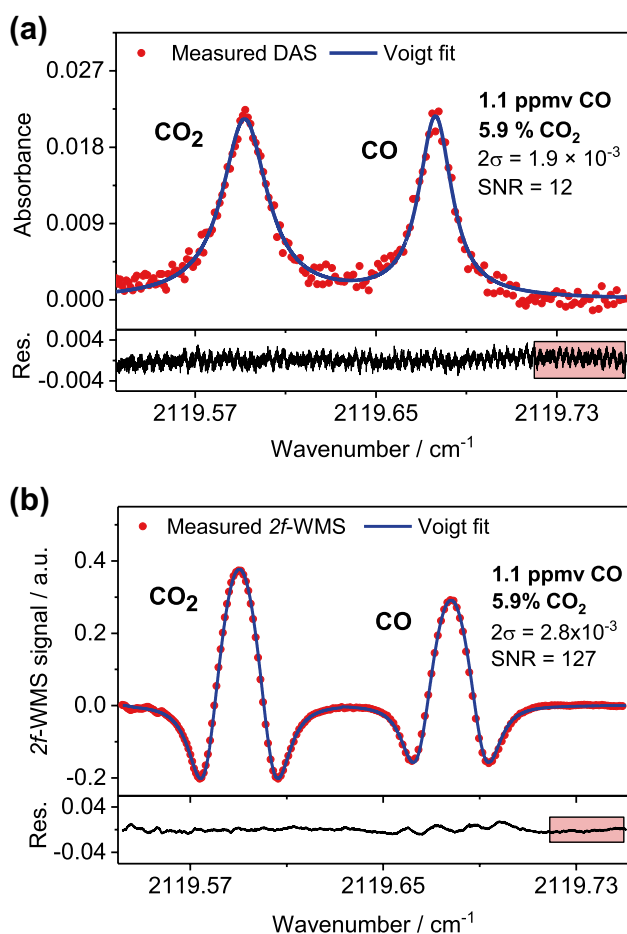


Fig. 4 Typical direct absorption (a) and $2f$ -wavelength modulation (b) spectra (pressure 100 Torr) of CO (1.1 ppmv) and CO₂ (5.9%) in breath recorded during online sampling with a rate of 7 Hz. Raw data (red solid markers) and Voigt least-squares fit (blue solid line) are shown with residual below. For clarity, only every 50th data point is shown in the spectra

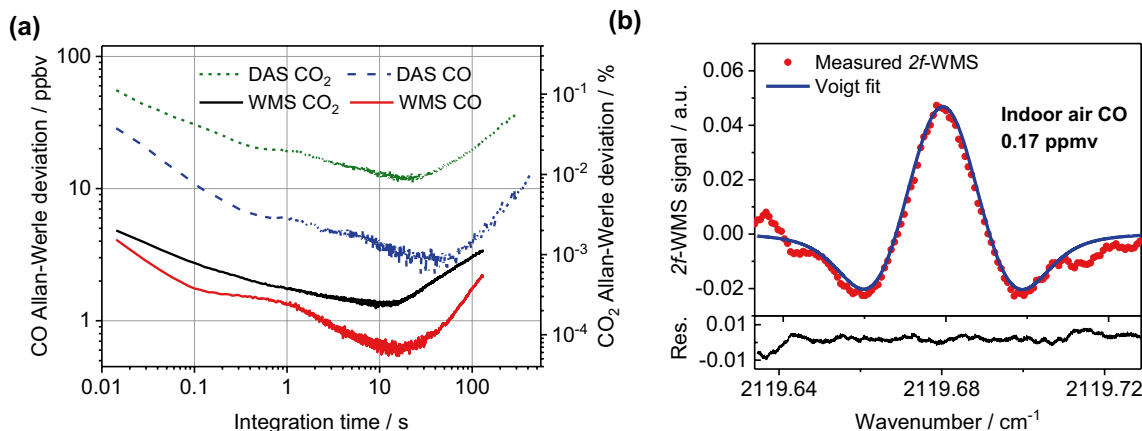


Fig. 5 a Allan-Werle deviation plots for CO and CO₂ detection with DAS and WMS. b Measured spectrum (red solid markers) of CO in indoor air (170 ppbv) with corresponding Voigt curve fit (blue solid

line) and residual shown below. For clarity, only every 30th data point is shown in the spectrum

detection method is around a factor of 10 more precise than DAS. The highest achievable precision for CO with the present WMS setup is 0.6 ppbv at 15 s averaging, and for CO₂ it is 2 ppmv at 12 s averaging. At the conditions of real-time detection with 10 averages and 7 points/s time-resolution, the precisions are 2 ppbv for CO and 7 ppmv for CO₂. Beyond 0.1 s averaging the curves do not follow the usual $1/f$ behavior due to the fluctuations in the WMS background. Sensitivity and precision are demonstrated by showing a typical $2f$ -WMS spectrum of CO in laboratory indoor air (Fig. 5b), which yielded a concentration of 170 ppbv.

The calibration curves displayed in Fig. 6 were obtained by dilution of the available CO and CO₂ gas standards with dry air. Figure 6a presents the CO calibration curve for DAS (triangular markers) and WMS (circular markers), together with a linear fit to the DAS data. Figure 6b presents the CO₂ calibration curve for DAS (triangular markers) and WMS (circular markers) with a second-order polynomial fit to the WMS data. For CO, the DAS signal (evaluated using the full Beer-Lambert law) is linear with concentration, whereas the $2f$ -WMS peak value levels off beyond the optical thin limit (absorbance >0.1). Thus, without correction, WMS is only used for CO concentrations below 5 ppm; otherwise DAS is employed. In the CO₂ calibration curve, although the absorbance is below 0.05, both DAS and WMS show the same, slightly nonlinear, concentration dependence. A second-order polynomial fit was applied to the data and the resulting function was used to evaluate the eCO₂ concentrations.

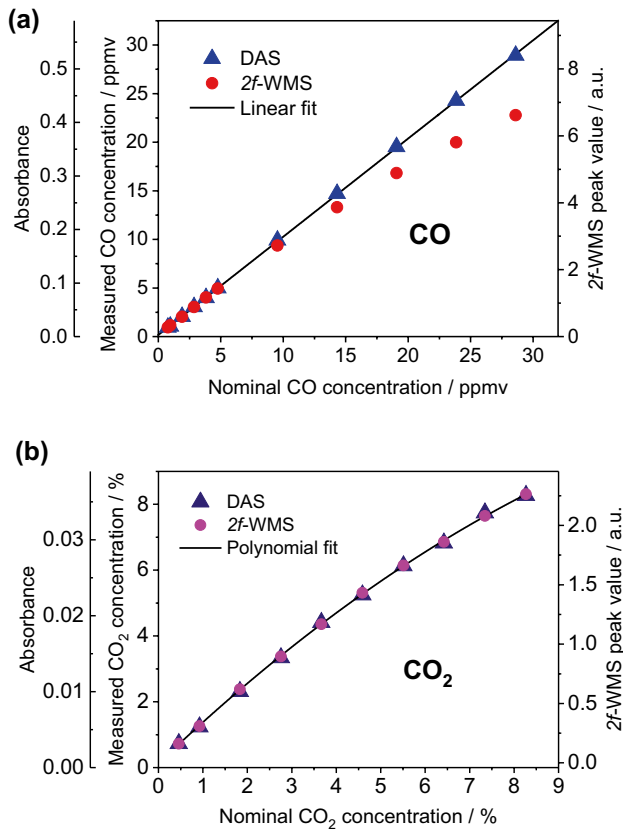


Fig. 6 Calibration curves for CO (a) and CO₂ (b) for DAS (triangular markers) and 2f-WMS (circular markers) detection. The solid lines show a linear curve fit to the DAS CO data, and a second-order polynomial fit to the CO₂ WMS data

5 Application to real-time breath gas analysis

The ability of the EC-QCL-based sensor to perform real-time BGA is demonstrated by measuring CO and CO₂ exhalation profiles of two male, healthy non-smokers (aged 37 and 41 years) under different conditions. In general, the subjects were sitting relaxed and performed tidal-breathing at a normal rate. No special pre-exhalation maneuver, such as deep inhalation or few-seconds breath holding, was used, except in the breath-holding experiments. Both inhalation and exhalation were conducted through the mouth (and the breath sampling system). The breathing frequency and exhalation volume were kept around 5–6 breaths/min and 800 ml, respectively, with the help of the visual indicators. The indoor air CO concentration was measured during the inhalation phase, when ambient air was sampled. Figure 7a shows sequences of four consecutive eCO (upper panel) and eCO₂ (lower panel) exhalation profiles detected simultaneously during free tidal breathing by one of the subjects. The eCO₂ traces measured by the capnograph (red dashed line) are shown in the lower panel for comparison.

The eCO₂ traces measured by TDLAS and capnography show identical concentrations and almost identical shape as can be seen in Fig. 7b, which compares the eCO and the two eCO₂ traces for one of the breath cycles in Fig. 7a. Time zero indicates the start of the exhalation, as recorded by the flow meter of the breath sampler. The figure also illustrates the three different exhalation phases expected for expirograms of biomarkers with low water solubility (negligible interaction between gas and airway lining fluids during exhalation), and little contribution from airway tissue

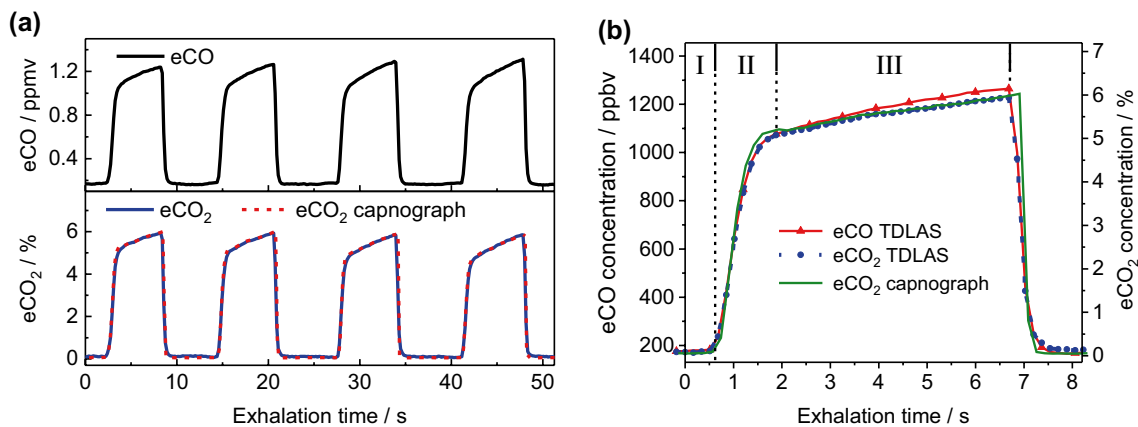


Fig. 7 a Sequences of real-time eCO (upper panel) and eCO₂ (lower panel) exhalation profiles from a healthy non-smoker. The eCO₂ profiles measured with capnography (red dashed line) are also shown. b Comparison between the CO and CO₂ expirograms for one of the

breath cycles. The three different exhalation phases are indicated. Time zero designates the start of the exhalation. For clarity, only every 4th data point is shown in the eCO profile. No data smoothing was applied

and oral/nasal cavity, such as CO and CO₂. Phase I represents air emptying the anatomic dead space (conducting airways), here equal to the inhaled CO concentration. Phase III constitutes the air from the alveoli, and denotes the alveolar slope, whereas the rapidly rising phase II of the expirogram represents the transition between phases I and III [30].

The CO₂ exhalation profiles show the same end-tidal concentration and have almost identical shape, which is a validation for the true real-time performance of the sensor. The slightly faster rise and later decline of the capnograph data compared to the TDLAS results are due to the different measurement locations, i.e. close to the mouth and in the MPC. Therefore, for all data shown, the time scale of the eCO profiles measured by TDLAS have been corrected for this slight delay. Interestingly, while the TDLAS measured CO and CO₂ profiles show the same rise and decay, the alveolar slope in phase III is slightly higher for CO.

Figure 8 presents results from measurements investigating the dependence of eCO expirograms on exhalation flow rate and breath-holding time for the two healthy non-smokers. In Fig. 8a, c, single breath cycles recorded with

three different exhalation flow rates at a constant exhalation volume (~800 ml) are shown. Again, time zero constitutes the start of the exhalation. With increasing flow rate, for both subjects, the total exhalation time becomes shorter, the alveolar slope larger, the end-tidal concentration lower and the sharp eCO increase of exhalation phase II occurs earlier. Figure 8b, d displays single eCO expirograms for five different breath-holding times, all recorded with similar exhalation flow rates, but slightly different exhalation volumes, as can be seen from the difference in exhalation time. For both subjects, with increasing breath-holding time, the rapid eCO increase of exhalation phase II happens earlier and is steeper. The eCO levels reach a plateau that is almost constant throughout phase III. The plateau and end-tidal concentrations are higher, and the alveolar slopes lower, the longer the breath-holding time. For 20 s breath-holding, the plateau exhibits a slightly negative slope.

In order to further illustrate the eCO flow rate dependence and to evaluate possible differences compared to eCO₂, the exhalation profiles shown in Fig. 8c (subject 2) and the corresponding eCO₂ profiles are plotted as a

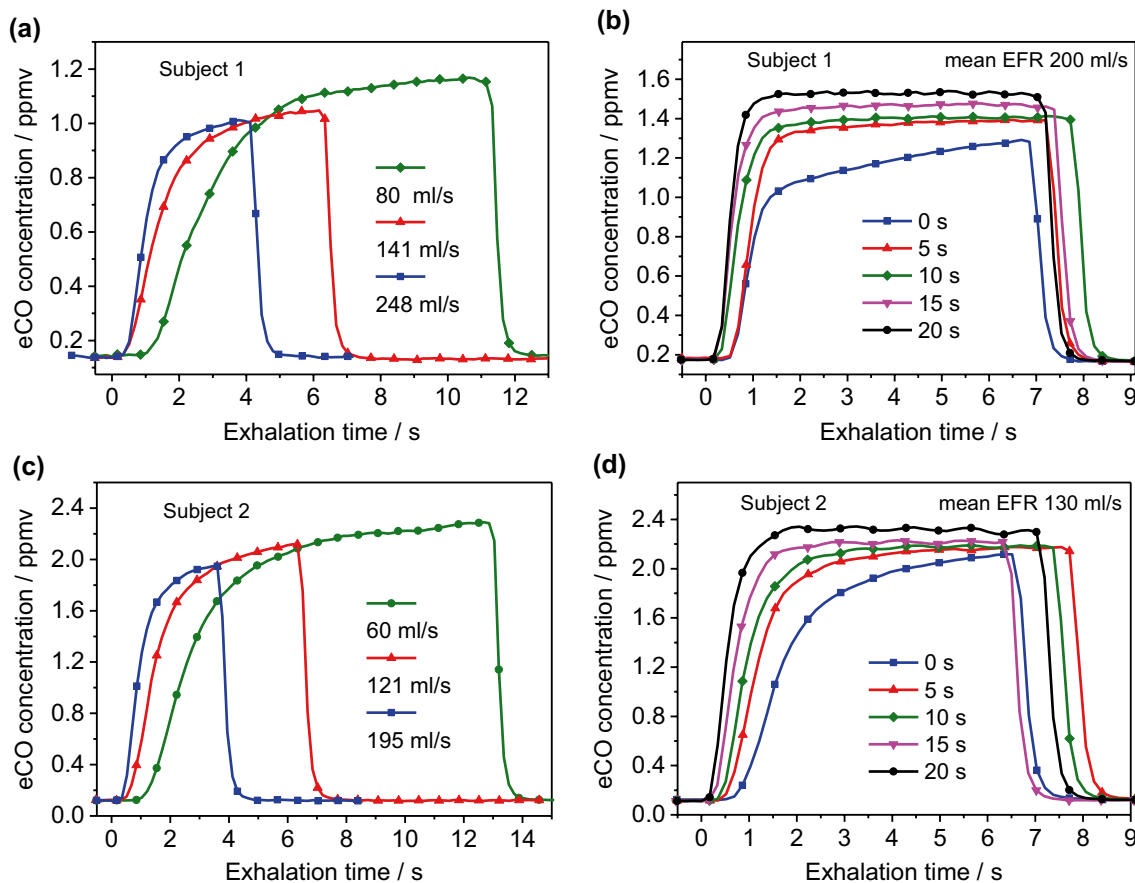


Fig. 8 Single eCO expirograms as a function of exhalation flow rate (a, c) and breath-holding time (b, d) for two healthy non-smokers. Time zero indicates the start of the exhalation. For clarity, only every

4th data point is shown. No data smoothing was applied. *EFR* exhalation flow rate

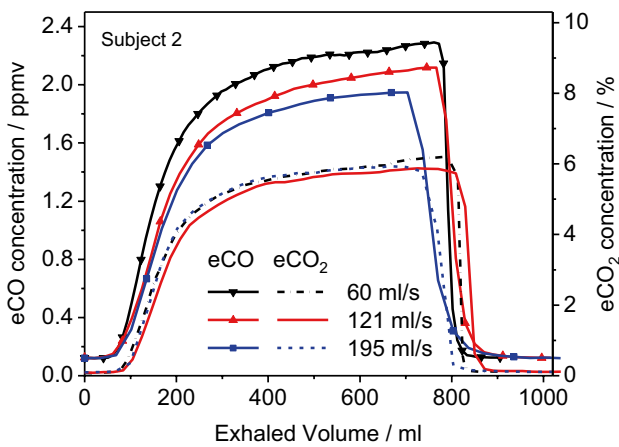


Fig. 9 Single eCO exhalation profiles from subject 2 (same data as in Fig. 8c) plotted as a function of exhaled volume, together with the corresponding eCO₂ expirograms (capnograph data)

function of exhaled volume in Fig. 9. The CO₂ expirograms are taken from the capnograph. As above, the capnography data show a slightly less steep decay at the end of exhalation, due to the measurement location close to the mouth. The CO₂ traces are very similar regarding phases I and II, alveolar slope and end-tidal concentration, and thus do not seem to exhibit a significant flow dependence. The eCO profiles, on the other hand, have a shorter phase I, a steeper rise during phase II and higher end-tidal concentrations with decreasing exhalation flow rate.

6 Discussion

The wide mode-hop-free tuning range of the EC-QCL allows for high-resolution broadband DAS, which can be useful for screening of breath samples and detection of larger volatile organic molecules, if the biomarkers occur in relatively high concentrations. In addition, it provides the possibility to find the most suitable wavelength range for narrowband detection and to perform narrowband scans in different spectral regions with the same laser. In the current setup, the sensitivity of broadband spectroscopy is limited by the poor sweep-to-sweep repeatability, which impairs averaging, absorbance calculation using the separately measured background signal and the accuracy of the frequency scale. The precision of the relative frequency scale could be improved by using two detectors and simultaneous detection of frequency scale and analytical signal. In general, the absorption contrast could be enhanced by using an MPC or optical cavity with longer effective path length.

The performance of narrowband WMS detection is comparable to recent EC-QCL-based WMS setups [8, 9, 12] and close to cavity-enhanced spectrometers [10, 13]. The

sensitivity was ultimately limited by fluctuations in the wavelength-dependent background caused by fringes. Due to the use of an MPC and WMS curve fitting, the sensitivity and precision of real-time eCO detection are at least a factor of ten better than those for typical single-pass WMS setups [33]. This results in more accurate and precise eCO expirograms and provides the possibility to quantify indoor air CO. In principle, calibration-free WMS with $2f/1f$ -detection and digital lock-in amplifiers [38] could be used to make the system more compact and avoid calibration procedures. However, this approach is slightly less sensitive than $2f$ -WMS with an external lock-in amplifier, since the modulated dc signal has to be acquired with high dynamic range, which limits the vertical resolution of the data acquisition system. For BGA, where the sample can be flown through a gas cell and analyzed under well-controlled conditions, and calibration curves can easily be measured, there is little advantage in employing $2f/1f$ -WMS.

The end-tidal eCO and eCO₂ concentrations measured in this study were in the range expected for healthy non-smokers, and the shape of the expirograms showed the three exhalation phases, as anticipated for biomarkers with low water-solubility. The fact that the eCO₂ profiles measured by capnography and laser spectroscopy were essentially equal confirms that the breath was sampled reliably and in real-time. The general similarity between the eCO and eCO₂ exhalation profiles indicates that the two molecules are comparable in terms of physiological and physical/chemical properties. Both have relatively low water-solubility (although the solubility of CO₂ is 40 times higher than that of CO) and gas exchange occurs mainly in the alveolar region. However, the CO₂ exhalation profiles have a smaller alveolar slope than eCO (Fig. 7b) and show only a weak dependence on flow rate (Fig. 9).

Importantly, it was found that eCO is affected by different exhalation flow rates and breath-holding times for healthy subjects. These dependencies are probably caused by the same underlying phenomenon. On an absolute time scale (Figs. 8a, c), the faster the exhalation the earlier will phase III be observed and the steeper will be the rise during phase II. However, relative to the total exhalation time (Fig. 9), for higher flow rate, there is less time for the CO-enriched alveolar air to mix (by axial diffusion) with dead space air, which results in a 'later' and less steep phase II and lower end-tidal eCO levels. This line of argumentation is confirmed by the observed dependence on breath-holding time (Figs. 8b, d). The longer the breath is held in the respiratory system, the more time there is for the alveolar, CO-enriched air to equilibrate with dead space air by axial diffusion. In addition, blood CO may constantly diffuse into the alveoli [33], which would explain the increasing phase III plateau and end-tidal concentrations that probably approach the alveolar CO concentration. A low exhalation

flow rate thus has a similar effect on the end-tidal concentrations as breath holding (Figs. 8c, d).

The results obtained in this study are in good agreement with the work by Fritsch et al., who employed highly sensitive cavity ring-down spectroscopy, and clearly observed a dependence on both flow rate and breath-holding time in healthy non-smokers and smokers [32]. However, the findings are partly in contrast to investigations by Zetterquist et al. [31] and Pakmanesh et al. [33], where only a dependence on breath-holding time was observed. Possible reasons for this discrepancy include differences in the breath sampling procedure and lack of sufficient sensitivity and real-time capability to precisely measure eCO expirograms and resolve the flow rate dependence.

The reason for the observed dependence of eCO on flow rate and breath-holding time is not clear. Gas exchange with the airway wall lining fluids is unlikely due to the low water-solubility of CO. One rationale is that blood CO is not in equilibrium with the lungs and CO is constantly diffusing into alveolar air [33], from where it is distributed to the respiratory tract by axial diffusion. However, there could also be CO release from tissue in lung or airways. The latter is supported by the fact that the eCO₂ dependence on flow rate is weak and that for 20 s breath-holding time, the maximum concentration occurs at the end of phase II, resulting in a negative alveolar slope. Coupling the experimental data to advanced physiological models and simulations of CO exhalation profiles could provide additional means to investigate the physiology of carbon monoxide.

7 Conclusions

We present a sensitive mid-infrared TDLAS sensor for real-time analysis of carbon monoxide and carbon dioxide in exhaled human breath. The instrument is based on an EC-QCL operating around 4.7 μm , a low-volume multipass cell and wavelength modulation spectroscopy. The capability to perform high-resolution broadband spectroscopy of breath samples was demonstrated. Using narrow-band WMS detection, the instrument allowed for simultaneous detection of CO and CO₂ expirograms with high precision and time-resolution, as well as quantification of indoor air CO. This proved useful in investigating the physiology of eCO. In particular, it was found that, in contrast to eCO₂, the eCO expirograms have a strong dependence on exhalation flow rate and breath-holding time for healthy non-smokers. The sensor opens up for detailed studies in physiology and toxicology, which may provide ways to distinguish between different endogenous and exogenous sources of eCO, including possible contributions due to respiratory diseases.

Acknowledgements This work was supported by the Swedish Research Council (621-2013-6031) and the Kempe Foundations (SMK-1446).

Open Access This article is distributed under the terms of the Creative Commons Attribution 4.0 International License (<http://creativecommons.org/licenses/by/4.0/>), which permits unrestricted use, distribution, and reproduction in any medium, provided you give appropriate credit to the original author(s) and the source, provide a link to the Creative Commons license, and indicate if changes were made.

References

1. R.F. Curl, F. Capasso, C. Gmachl, A.A. Kosterev, B. McManus, R. Lewicki, M. Pusharsky, G. Wysocki, F.K. Tittel, *Chem. Phys. Lett.* **487**, 1 (2010)
2. T.H. Risby, F.K. Tittel, *Opt. Eng.* **49**, 111123 (2010)
3. A. Manninen, B. Tuzson, H. Looser, Y. Bonetti, L. Emmenegger, *Appl. Phys. B* **109**, 461 (2012)
4. P. Kluczynski, J. Gustafsson, A.M. Lindberg, O. Axner, *Spectrochim. Acta B* **56**, 1277 (2001)
5. B.E. Brumfield, M.S. Taubman, J.D. Suter, M.C. Phillips, *Opt. Express* **23**, 25553 (2015)
6. A. Lambrecht, M. Pfeifer, W. Konz, J. Herbst, F. Axtmann, *Analyst* **139**, 2070 (2014)
7. M.C. Phillips, M.S. Taubman, B.E. Bernacki, B.D. Cannon, R.D. Stahl, J.T. Schiffert, T.L. Myers, *Analyst* **139**, 2047 (2014)
8. G. Hancock, J.H. van Helden, R. Peverall, G.A.D. Ritchie, R.J. Walker, *Appl. Phys. Lett.* **94**, 201110 (2009)
9. X. Chao, J.B. Jeffries, R.K. Hanson, *Appl. Phys. B* **106**, 987 (2011)
10. J.H. van Helden, N. Lang, U. Macherius, H. Zimmermann, J. Röpcke, *Appl. Phys. Lett.* **103**, 131114 (2013)
11. K. Wörle, F. Seichter, A. Wilk, C. Armacost, T. Day, M. Godejohann, U. Wachter, J. Vogt, P. Radermacher, B. Mizaikoff, *Anal. Chem.* **85**, 2697 (2013)
12. Y. Yu, N.P. Sanchez, R.J. Griffin, F.K. Tittel, *Opt. Express* **24**, 10391 (2016)
13. R. Centeno, J. Mandon, F.J. Harren, S.M. Cristescu, *Photonics* **3**, 22 (2016)
14. L. Dong, R. Lewicki, K. Liu, P. Buerki, M. Weida, F. Tittel, *Appl. Phys. B* **107**, 275 (2012)
15. T.H. Risby, S.F. Solga, *Appl. Phys. B* **85**, 421 (2006)
16. A. Amann and D. Smith: *Volatile biomarkers: non-invasive diagnosis in physiology and medicine* (Elsevier, 2013)
17. K.K. Chow, M. Short, H. Zeng, *Biomed. Spectrosc. Imaging* **1**, 339 (2012)
18. C. Di Natale, R. Paolesse, E. Martinelli, R. Capuano, *Anal. Chim. Acta* **824**, 1 (2014)
19. C.J. Wang, P. Sahay, *Sensors* **9**, 8230 (2009)
20. J. King, K. Unterkofler, G. Teschl, S. Teschl, H. Koc, H. Hinterhuber, A. Amann, *J. Math. Biol.* **63**, 959 (2011)
21. N.M. Tsoukias, H.-W. Shin, A.F. Wilson, S.C. George, *J. Appl. Physiol.* **91**, 477 (2001)
22. W. Miekisch, J.K. Schubert, *Trac-Trend. Anal. Chem.* **25**, 665 (2006)
23. J. Beauchamp, F. Kirsch, A. Buettner, *J. Breath Res.* **4**, 026006 (2010)
24. K.D. Skeldon, C. Patterson, C.A. Wyse, G.M. Gibson, M.J. Padgett, C. Longbottom, L.C. McMillan, *J. Opt. A-Pure Appl. Opt.* **7**, S376 (2005)

25. I. Ventrillard-Courtillot, T. Gonthiez, C. Clerici, D. Romanini, J. Biomed. Opt. **14**, 064026 (2009)
26. M. Metsälä, F.M. Schmidt, M. Skytta, O. Vaittinen, L. Halonen, J. Breath Res. **4**, 046003 (2010)
27. B. Cummings, M.L. Hamilton, L. Ciaffoni, T.R. Pragnell, R. Peverall, G.A. Ritchie, G. Hancock, P.A. Robbins, J. Appl. Physiol. **111**, 303 (2011)
28. S.W. Ryter, A.M.K. Choi, J. Breath Res. **7**, 017111 (2013)
29. E.O. Owens, Clin. Biochem. **43**, 1183 (2010)
30. J.C. Anderson, M.P. Hlastala, Pulm. Pharmacol. Ther. **20**, 112 (2007)
31. W. Zetterquist, H. Marteus, M. Johannesson, S. Nordvall, E. Ihre, J. Lundberg, K. Alving, Eur. Respir. J. **20**, 92 (2002)
32. T. Fritsch, P. Hering, M. Mürtz, J. Breath Res. **1**, 014002 (2007)
33. N. Pakmanesh, S.M. Cristescu, A. Ghorbanzadeh, F.J. Harren, J. Mandon, Appl. Phys. B **122**, 1 (2016)
34. J.H. Shorter, D.D. Nelson, J.B. McManus, M.S. Zahniser, S.R. Sama, D.K. Milton, J. Breath Res. **5**, 037108 (2011)
35. M. Sowa, M. Murtz, P. Hering, J. Breath Res. **4**, 047101 (2010)
36. L.S. Rothman, I.E. Gordon, Y. Babikov, A. Barbe, D. Chris Benner, P.F. Bernath, M. Birk, L. Bizzocchi, V. Boudon, L.R. Brown, A. Campargue, K. Chance, E.A. Cohen, L.H. Coudert, V.M. Devi, B.J. Drouin, A. Fayt, J.M. Flaud, R.R. Gamache, J.J. Harrison, J.M. Hartmann, C. Hill, J.T. Hodges, D. Jacquemart, A. Jolly, J. Lamouroux, R.J. Le Roy, G. Li, D.A. Long, O.M. Lyulin, C.J. Mackie, S.T. Massie, S. Mikhailenko, H.S.P. Müller, O.V. Naumenko, A.V. Nikitin, J. Orphal, V. Perevalov, A. Perrin, E.R. Polovtseva, C. Richard, M.A.H. Smith, E. Starikova, K. Sung, S. Tashkun, J. Tennyson, G.C. Toon, V.G. Tyuterev, G. Wagner, J. Quant. Spectrosc. Radiat. Transf. **130**, 4 (2013)
37. J. Westberg, J. Wang, O. Axner, J. Quant. Spectrosc. Ra. **113**, 2049 (2012)
38. Z. Qu, R. Ghorbani, D. Valiev, F.M. Schmidt, Opt. Express **23**, 16492 (2015)